Analysis of Circularly Polarized CTS Arrays — Source link ↗

Michele Del Mastro, Francesco Foglia Manzillo, David Gonzalez-Ovejero, Maciej Smierzchalski ...+4 more authors

Institutions: University of Rennes, Direction générale de l'armement

Related papers:

- Modeling of circularly-polarized CTS arrays

- Design and fabrication of a waveguide two-dimensional slot array with low sidelobe level of −35dB

- A novel edge wall waveguide slot antenna

- Isolation Enhancement Between Waveguide Slot Arrays Using Quasi-Gap Waveguide Structure

- Corner-fed microstrip antenna element and arrays for dual-polarization operation

Analysis of Circularly-Polarized CTS Arrays

M. del Mastro, F.F. Manzillo, D. Gonzalez-Ovejero, M. Smierzchalski, P. Pouliguen, P. Potier, R. Sauleau, M. Ettorre

Analysis of Circularly-Polarized CTS Arrays

Michele Del Mastro, Francesco Foglia Manzillo, *Member, IEEE*, David González-Ovejero, *Senior Member, IEEE*, Maciej Śmierzchalski, Philippe Pouliguen, Patrick Potier, Ronan Sauleau, *Fellow, IEEE*, and Mauro Ettorre, *Senior Member, IEEE*

Abstract—**This paper presents an efficient analysis method for a novel continuous transverse stub (CTS) antenna. As opposed to state-of-the-art CTS antenna designs, the proposed architecture achieves circular polarization using a single CTS array and without any polarization converter. The structure consists of long radiating slots/stubs fed by over-moded parallel-plate waveguides. More precisely, the transverse electromagnetic (TEM) mode and the first transverse electric (TE$_1$) mode of the feeding waveguides are used to generate a circularly-polarized field. The array is analyzed using a spectral mode-matching method. First, the active reflection coefficient of the infinite array is derived in closed form. A windowing approach is then adopted to compute the radiation patterns of finite-size arrays. Numerical results obtained with this method are in excellent agreement with full-wave simulations, carried out with a commercial software. The performance of this class of CTS antennas has been investigated using the developed model. It is theoretically demonstrated that the proposed array can be designed to attain an axial-ratio (AR) lower than 3 dB over a 52.9% relative bandwidth at broadside. Furthermore, the active input reflection coefficient is lower than -10 dB over a 40.8% relative bandwidth when the array steers its main beam at $\theta_0 = 45°$. This solution is an attractive candidate for next generation satellite communication terminals.**

Index Terms—**Continuous transverse stub array, circular polarization, oversized parallel-plate waveguides.**

I. INTRODUCTION

THE growth of satellite communication (Satcom) applications in Ka-band has boosted the development of novel antenna solutions with wide-band performance, wide-angle scanning capabilities, and low-form factor [1]. Continuous transverse stub (CTS) arrays have received particular attention from the community due to their low profile and wideband performance [2]–[4]. They consist of arrays of stubs or open-ended parallel-plate waveguides (PPWs), which radiate in free space and may be fed either in series or in parallel. A series-fed CTS array [5] comprises stubs, finite in height, placed on the upper plate of a PPW. The beam is spatially steered by varying the angle of incidence of the wave launched into the

feeding PPW. On the other hand, standard parallel-fed CTS arrays [6], [7] adopt long slots in a metallic plane fed by a corporate network of mono-modal PPWs, supporting the TEM mode. Such network typically excites with the same amplitude and phase each slot. The parallel-fed architecture exhibits very wide-band capabilities owing to the mutual coupling of the slots [8].

However, the main drawback of CTS arrays is that, due to their radiation mechanism, they are inherently linearly-polarized. Circular-polarization (CP) has become an essential feature for Satcom applications for enhancing the robustness of the satellite communication links [9]. Existing solutions to achieve CP typically rely on add-on linear-to-circular (LP-to-CP) converters, placed in proximity of the radiating slots [10], [11]. Nevertheless, the use of LP-to-CP converters impacts on the overall size and thickness of the antenna system and, at the same time, introduces additional losses.

A novel concept is here proposed for CTS arrays. The main underlying idea is based on the bi-modal operation of the antenna. Over-moded PPWs are employed to feed the radiating elements. In particular, both the slots and PPWs should support the fundamental TEM and the first transverse electric (TE$_1$) modes. The transverse electric fields of these two modes are orthogonally-polarized and therefore, if properly excited, are able to radiate a CP field. This novel CTS architecture relies on a single radiating aperture, rather than on two arrays geometrically-organized in an egg-crate configuration, as recently proposed in [12]. Indeed, the radiating aperture in [12] consists of orthogonally-oriented long slots, series-fed by a corporate network of mono-modal PPWs. Thus, the radiation mechanism of the CTS antenna that we propose may provide CP fields resorting to a single aperture, which supports two orthogonally-polarized modes.

An efficient numerical tool is crucial to explore the potential of the structure described above. The proposed analysis method is based on a spectral mode-matching technique (MMT). This numerical tool builds on the work in [13], extending it to over-moded CTS arrays. In particular, the model provides a closed-form expression for the active impedance of an infinite array excited by the TE$_1$ mode. The active impedance under TEM mode operation is also accurately predicted for slots and PPWs supporting the two selected modes, which also constitutes a futher new contribution with respect to [13]. Furthermore, the radiation patterns of finite-size arrays are derived using a windowing approach. Design guidelines are also discussed for achieving a wideband impedance matching and low axial-ratio (AR). Several examples are presented to provide the reader with an useful deepening for different design goals arising in practical applications. The insight pro-

(a) Perspective view.
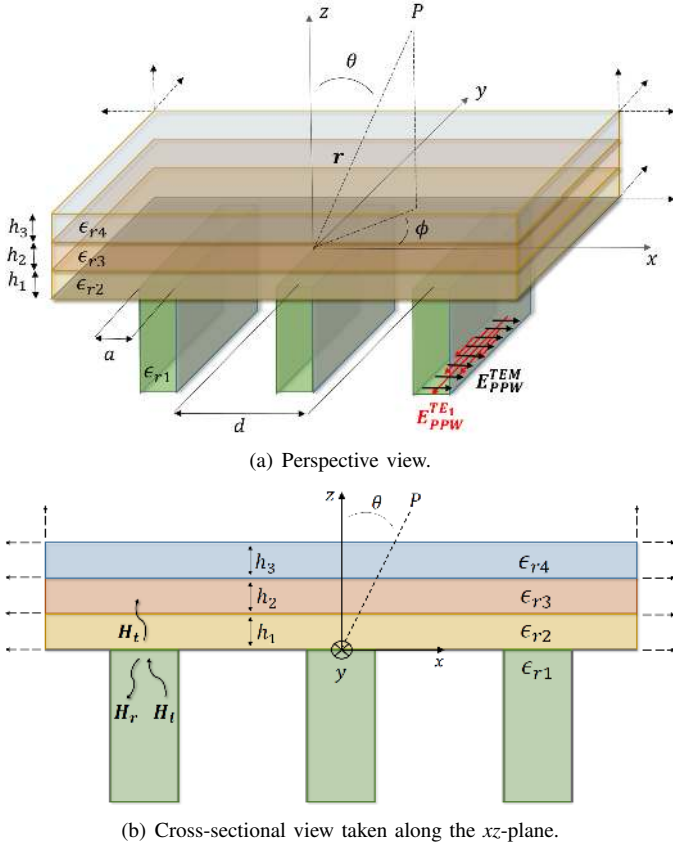

(b) Cross-sectional view taken along the xz-plane.

Fig. 1. Geometry of the problem. Only three dielectric slabs are shown for the layered media for the sake of clarity.

vided by the proposed analysis is of considerable importance on the study of the antenna's potentialities and limitations. The versatility of the tool to analyze the array under different and precisely controlled excitations (single-mode, multimode) is fundamental to perform fast and accurate parametric studies. The impact of the array parameters on the antenna's matching and radiation performance are exhaustively displayed and discussed, thus easing the design of a circularly-polarized SatCom terminal antenna.

The paper is organized as follows. In Section II, the active impedance of the radiating slots is derived for an infinite circularly-polarized CTS array under both TEM and TE_1 mode operation. In Section III, numerical results are validated by comparison with full-wave simulations. In Section IV, radiation properties and AR performance for a finite-size array are derived. In Section V, design guidelines are outlined. Furthermore, Section VI shows a representative example of a possible design in Ka-band. Finally, Section VII concludes the paper.

II. ANALYTICAL MODEL

Fig. 1 shows the geometry of the problem under consideration. An infinite array of slots on a ground plane is fed by over-moded PPWs. The width of the slots is a and they are infinitely-extended along the y-axis. In order to guarantee a bi-modal behavior of the PPWs, we restrict our analysis to values of a between $\lambda/2$ and λ, where λ is the operating wavelength

in the medium filling the PPWs. The inter-element spacing along the x-axis is d. The PPWs are filled with a material of permittivity ϵ_{r1}. The modes are considered propagating along the z-axis. The metallic parts are considered lossless and, hence, modeled as perfect-electric conductor (PEC). The slots radiate into a planar multi-layered medium. The number of media can be arbitrarily chosen and their height is indicated by h_q with $q \in \mathbb{N}^+$. Each medium has permittivity $\epsilon_{r,q+1}$, where $q \in \mathbb{N}^+$.

By virtue of the equivalence theorem, a magnetic field integral equation (MFIE) is derived to formulate the electromagnetic problem by enforcing the continuity of the tangential component of the magnetic field on the slots:

$$\hat{z} \times [\mathbf{H_i}(x,y,z) + \mathbf{H_r}(x,y,z) - \mathbf{H_t}(x,y,z)]\,|_{on\,\mathfrak{D}} = \mathbf{0} \quad (1)$$

where $\mathfrak{D} = \{(x,y,z) \in \mathbb{R}^3 : nd < x < a + nd$ with $n \in \mathbb{Z}, -\infty < y < +\infty, z = 0\}$.

In (1), $\mathbf{H_i}(x,y,z)$, $\mathbf{H_r}(x,y,z)$, and $\mathbf{H_t}(x,y,z)$ are, respectively, the incident, reflected and transmitted magnetic field at the discontinuity $z = 0$. A simple graphical representation of the fields is shown in Fig. 1(b). The two incident fields are given by

$$\mathbf{H_i^{TEM}} = \sum_{n=-\infty}^{+\infty} \mathbf{H_{PPW}^{TEM}}(x-nd, y)\textstyle\prod_a\left(x - \tfrac{a}{2} - nd\right)e^{-ik_{x0}nd} \quad (2)$$

$$\mathbf{H_i^{TE_1}} = \sum_{n=-\infty}^{+\infty} \mathbf{H_{PPW}^{TE1}}(x-nd, y)\textstyle\prod_a\left(x - \tfrac{a}{2} - nd\right)e^{-ik_{x0}nd} \quad (3)$$

when the array is excited by a TEM or a TE_1 mode, respectively. In turn, the expressions for the reflected and transmitted fields are

$$\mathbf{H_r} = -\sum_{n=-\infty}^{+\infty} \mathbf{H_{PPW}}(x-nd, y)\textstyle\prod_a\left(x - \tfrac{a}{2} - nd\right)e^{-ik_{x0}nd} \quad (4)$$

$$\mathbf{H_t} = \int_{\mathbb{R}^2} \underline{\underline{G_t^{HM}}}\left(x-x', y-y'\right)\mathbf{M_t}\left(x', y'\right)dx'dy' \quad (5)$$

where $\prod_a(x) = 1$ for $-a/2 < x < a/2$ and null elsewhere, $k_{x0} = k_0 \sin\theta_0 \cos\phi_0$ with (θ_0, ϕ_0) the beam pointing direction, and $\mathbf{M_t}(x,y,z)$ is the transverse magnetic distribution on $\mathfrak{D}$ and its expression can be found in [13]. Furthermore, $\underline{\underline{G_t^{HM}}}$ is the transverse dyadic Green's function for the half-space over the slots. The latter may be evaluated in the presence of a layered medium using an equivalent transmission-line model as in [14]. The extended forms of $\mathbf{H_{PPW}^{TEM}}$, $\mathbf{H_{PPW}^{TE_1}}$, and $\mathbf{H_{PPW}}$ in (2), (3), and (4), respectively, are provided in [13]. It is important to notice that only the TEM and TE_1 mode excitations are considered in (2) and (3) for the incident field even if, since $\lambda/2 < a < \lambda$, the TM_1 mode can propagate as well. Since possible mutual couplings between TEM and TM_1 modes may occur along any eventual discontinuities, a possible solution to cut-off the TM_1 mode relies on feeding the slots with longitudinally-corrugated PPWs [21]–[25]. In the following we will exclude the TM_1 mode to feed the structure.

By replacing (2) or (3), (4), and (5) in (1), a MFIE is obtained. This equation can be approximately solved by

This article has been accepted for publication in a future issue of this journal, but has not been fully edited. Content may change prior to final publication. Citation information: DOI 10.1109/TAP.2020.2972438, IEEE Transactions on Antennas and Propagation

3

truncating the series to 2M-1 PPW's modes and $2N_f+1$ Floquet's modes, and applying the Galerkin's method to (1). Two different linear problems arise for the two selected modes. For each mode, the matrix-based form yields

$$\begin{bmatrix} \underline{\underline{Y}}^{TE,TE} & \underline{\underline{Y}}^{TE,TM} \\ \underline{\underline{Y}}^{TM,TE} & \underline{\underline{Y}}^{TM,TM} \end{bmatrix} \begin{bmatrix} \mathbf{V^{TE}} \\ \mathbf{V^{TM}} \end{bmatrix} = \begin{bmatrix} \mathbf{I_{01}} \\ \mathbf{I_{02}} \end{bmatrix} \quad (6)$$

where $\mathbf{V^{TE}} = \left[V_0^{TE}, V_1^{TE}, \ldots, V_{M-1}^{TE}\right]$ and $\mathbf{V^{TM}} = \left[V_1^{TM}, \ldots, V_{M-1}^{TM}\right]$ are the scalar mode functions of TE and TM modes in the PPWs, respectively. Depending on the type of impinging field we consider (i.e., TEM (2) or TE_1 (3)), the known terms $\mathbf{I_{01}}$ and $\mathbf{I_{02}}$ take a different form. The mathematical expression of the admittance matrix in (6) can be found in [13].

A. Active admittance for TEM-excitation

For completeness, we report the main results for the TEM mode given in [13]. The constant term in (6) is given by

$$\mathbf{I_{01}} = \begin{bmatrix} iV_{inc}^{TEM}\sqrt{a}Y_0^{TE} \\ 0 \\ \vdots \\ 0 \end{bmatrix}, \quad \mathbf{I_{02}} = \begin{bmatrix} 0 \\ \vdots \\ 0 \end{bmatrix} \quad (7)$$

where $V_{inc}^{TEM} = 1\,(V/\sqrt{m})$ and $Y_0^{TE} = 1/\zeta$ with ζ the intrinsic impedance of the medium inside the PPWs. By inverting (6), the scalar mode functions $V_{m=0,\ldots,M-1}^{TE}$ and $V_{m=1,\ldots,M-1}^{TM}$ can be calculated and the fields on the aperture expressed in a closed-form. The active admittance of the radiating slots can be then derived. The mathematical expression of the normalized active admittance is given by

$$\bar{Y}_{act}^{TEM} = -\frac{1}{\left|V_0^{TE}\sqrt{a}\right|^2} \int_{\mathfrak{D}} \mathbf{H_t} \cdot \mathbf{M_{t,\,TEM}^*}\,dxdy \quad (8)$$

$$\mathbf{M_{t,\,TEM}} = -\frac{iV_0^{TE}}{\sqrt{a}}\Pi_a\left(x - \tfrac{a}{2}\right)e^{-k_{y0}y}\hat{y} \quad (9)$$

In (8), $\mathbf{H_t}$ takes into account the contribution of all higher order modes in the PPWs and the mutual coupling among feeding waveguides (see (5)). In (9) $\mathbf{M_{t,\,TEM}}$ considers only the effect of the fundamental mode within the PPWs.

The extended form of the normalized active admittance (8) is given in [13].

B. Active admittance for TE_1-excitation

When the array is excited by a TE_1 mode, the incident fields are expressed by (3). In this case, the known term of the linear system (6) is given by

$$\mathbf{I_{01}} = \begin{bmatrix} 0 \\ \frac{V_{inc}^{TE_1}Y_1^{TE}}{k_1^{TE}}\frac{\pi}{\sqrt{2a}} \\ 0 \\ \vdots \\ 0 \end{bmatrix}, \quad \mathbf{I_{02}} = \begin{bmatrix} \frac{iV_{inc}Y_1^{TE}}{k_1^{TE}}\frac{2k_{y0}}{\sqrt{a}} \\ 0 \\ \vdots \\ 0 \end{bmatrix} \quad (10)$$

where $V_{inc}^{TE_1} = 1\,V/\sqrt{m}$, $Y_1^{TE} = \sqrt{k^2 - \left(k_1^{TE}\right)^2}/(\zeta k)$, and $k_1^{TE} = \sqrt{(\pi/a)^2 + k_{y0}^2}$ with $k_{y0} = k_0\sin\theta_0\sin\phi_0$, whereas

k_0 and k are wave-numbers in free space and in the medium inside the PPWs, respectively. In (10), the non-null entry of $\mathbf{I_{02}}$ takes into account the coupling between TE and TM modes which occurs when the antenna beam is steered in planes $\phi \neq \{0°, 180°\}$.

As for TEM mode, by solving (6) the scalar mode functions $V_{m=0,\ldots,M-1}^{TE}$ and $V_{m=1,\ldots,M-1}^{TM}$ are found. The electromagnetic field on the plane of the slots is therefore completely determined. The active admittance can be then expressed as

$$\bar{Y}_{act}^{TE_1} = -\frac{1}{\left|V_1^{TE}\sqrt{a}\right|^2} \int_{\mathfrak{D}} \mathbf{H_t} \cdot \mathbf{M_{t,\,TE1}^*}\,dxdy \quad (11)$$

where

$$\mathbf{M_{t,\,TE1}} = M_{t,TE_1}^x\hat{x} + M_{t,TE_1}^y\hat{y} \quad (12)$$

with

$$M_{t,TE_1}^x = -\sqrt{\frac{2}{a}}\frac{\frac{\pi}{a}V_1^{TE}e^{-ik_{y0}y}}{\sqrt{k_{y0}^2 + (\pi/a)^2}}\sum_{n=-\infty}^{+\infty}\sin\left(\frac{\pi}{a}(x - nd)\right)$$
$$\times \Pi_a\left(x - \tfrac{a}{2} - nd\right)e^{-ik_{x0}nd} \quad (13)$$

$$M_{t,TE_1}^y = -\sqrt{\frac{2}{a}}\frac{ik_{y0}V_1^{TE}e^{-ik_{y0}y}}{\sqrt{k_{y0}^2 + (\pi/a)^2}}\sum_{n=-\infty}^{+\infty}\cos\left(\frac{\pi}{a}(x - nd)\right)$$
$$\times \Pi_a\left(x - \tfrac{a}{2} - nd\right)e^{-ik_{x0}nd} \quad (14)$$

The complete expression the active admittance (11) is given in Appendix A.

III. NUMERICAL RESULTS

The model presented in Section II allows to compute the active impedance per unit length $Z_{act} = 1/\bar{Y}_{act}$. The obtained results have been extensively validated by using a commercial full-wave simulator (i.e., CST STUDIO SUITE® [32]). The simulation setup is shown in Fig. 2. A waveguide port is used to launch the TEM and TE_1 modes into the radiating slot, respectively. Furthemore, a Floquet's port is considered on the top of the air-box, placed above the radiating slot. Unit-cell boundary conditions are enforced on the lateral faces of the model. The reference plane of the derived active
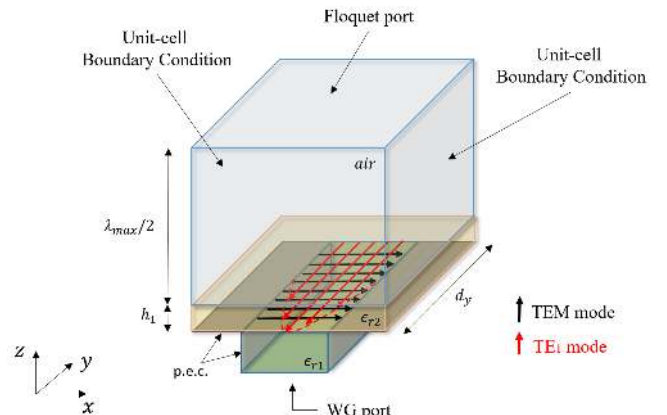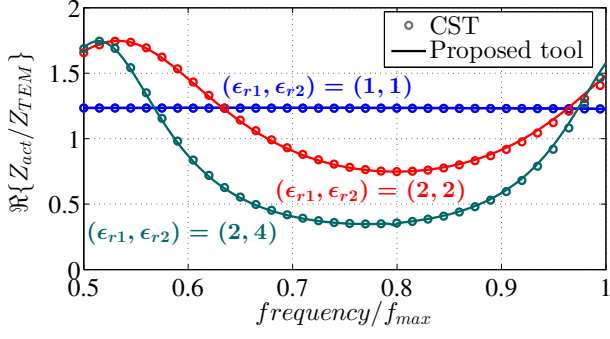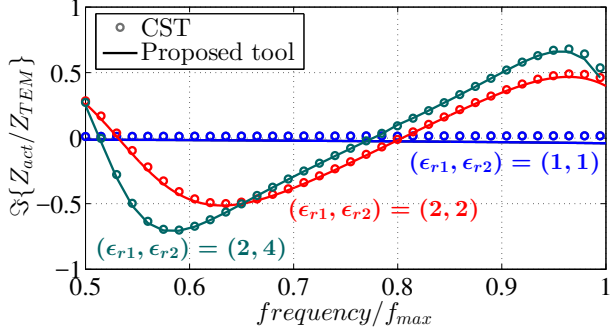

Fig. 2. Simulation setup of the CTS array unit-cell. The structure is periodic along x- and y-axes.

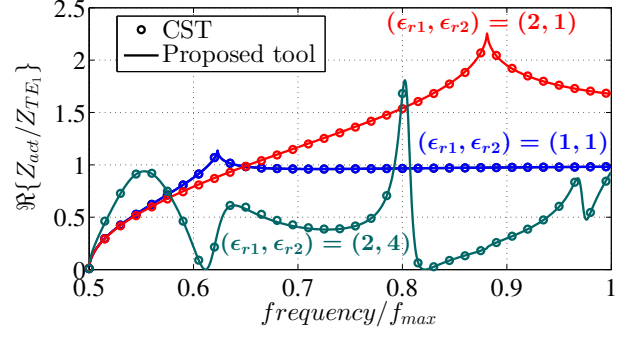(a) Real part of the active impedance versus frequency.

(b) Imaginary part of the active impedance versus frequency.

Fig. 3. Active impedance for TEM-mode excitation versus frequency along the plane at $\phi = 90°$ for $\theta_0 = 30°$. The parameters used in the simulation are $a = 0.5c/(f_{min}\sqrt{\epsilon_{r1}})$, $d = 1.07a$, $h = 0.5c/(f_{min}\sqrt{\epsilon_{r2}})$, and $Z_{TEM} = \zeta$.

(a) Real part of the active impedance versus frequency.

(b) Imaginary part of the active impedance versus frequency.

Fig. 4. Active impedance for TE_1-mode excitation versus frequency along the plane at $\phi = 0°$ for $\theta_0 = 30°$. The parameters used in the simulation are $a = 0.5c/(f_{min}\sqrt{\epsilon_{r1}})$, $d = 1.07a$, $h = 0.5c/(f_{min}\sqrt{\epsilon_{r2}})$, and $Z_{TE_1} = 1/Y_1^{TE}$.
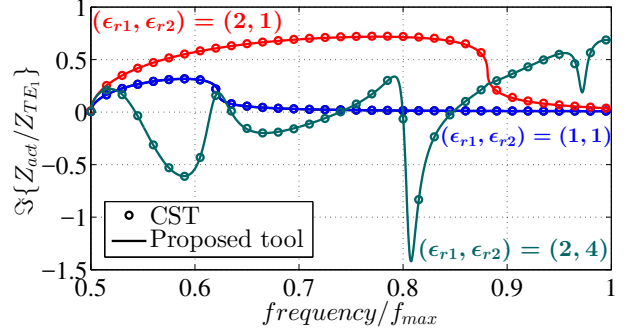
parameters is located over the slot. The main parameters of the structure are set as $f_{min} = f_{cut-off}^{TE_1}$, $f_{max} = 2f_{min}$, and $a = 0.5c/(f_{min}\sqrt{\epsilon_{r1}})$. These settings guarantee that only the fundamental (i.e., TEM) and the first two higher order modes (i.e., TE_1 and TM_1) can propagate into the PPWs. Furthermore, only one dielectric layer is considered over the slots with an arbitrary height $h_1 = 0.5c/(f_{min}\sqrt{\epsilon_{r2}})$. Finally, the spatial periodicity of the array is $d = 1.07a$ and the length of the slot is $d_y = \lambda_{max}/30$. Note that CTS arrays are one-dimensional periodic structure based on long slots. In this case, such a very small periodicity along the slot is only used to numerically-validate the proposed tool and avoid possible artifacts due to periodicity along the slot using [32]. Several combinations of ϵ_{r1} and ϵ_{r2} have been considered in order to validate the numerical tool and provide some design guidelines in various scenarios.

A. TEM-mode excitation

The TEM case is here considered since the results in [13] were validated only for single-mode PPWs, i.e. for $a < \lambda/2$. The number of Floquet's modes required to get a stable convergence is $N_f = 10$, while the number of PPW's modes is $M \geq 5$ both for the E-plane (i.e., $\phi = 0°$) and the H-plane (i.e., $\phi = 90°$). The real and the imaginary parts of the normalized active impedance versus frequency are shown in Fig. 3 along the H-plane. An excellent agreement is observed between the proposed tool and full-wave results.

Similar results are obtained along the E-plane and are not reported for the sake of brevity. Finally, it is important to note that the active S-parameter corresponding to the case $\epsilon_{r1} = \epsilon_{r2} = 1$ is less than -10 dB over a 66.6% band along the H-plane (i.e., for $\phi = 90°$) when the array is pointing at $\theta_0 = 30°$.
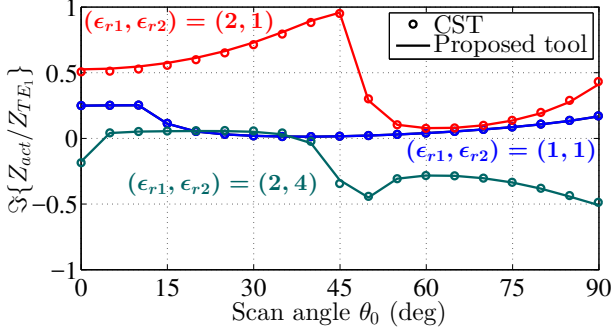
B. TE_1-mode excitation

In this subsection, we validate the active impedance calculation for the TE_1-excitation. Fig. 4 depicts the real and imaginary parts of the normalized active impedance versus frequency along the plane $\phi = 0°$. An excellent agreement is observed also in this case between the proposed numerical tool and full-wave results. One gets stable convergence for all the cases in Fig. 3 considering $M \geq 8$ and $N_f \geq 10$. This method has been validated for several combinations of ϵ_{r1} and ϵ_{r2}, showing always an excellent agreement in comparison to full-wave results. For the sake of completeness, Fig. 5 plots real and imaginary parts of the active impedance, normalized to the wave impedance $Z_{TE_1} = 1/Y_{TE_1}$ of the TE_1 mode versus the scan angles along the plane $\phi = 0°$ at $f_0 = (f_{min} + f_{max})/2$.

Finally, we also report the active S-parameter $S_{act} = (Z_{act} - aZ_{TE_1})/(Z_{act} + aZ_{TE_1})$ along the E-plane (i.e., $\phi = 90°$) versus frequency (see Fig. 6(a)) and scan angles θ_0 (see Fig. 6(b)). A stable convergence has been achieved by considering $M \geq 10$ PPW's modes and $N_f = 10$ Floquet's
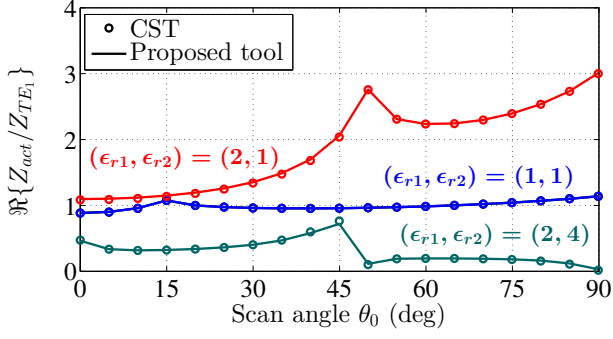
(a) Real part of the active impedance versus scan angles θ.

(b) Imaginary part of the active impedance versus scan angles θ.

Fig. 5. Active impedance for TE_1-mode excitation versus scan angles θ_0 along the plane $\phi = 0°$ at $f_0 = (f_{min} + f_{max})/2$. The parameters used in the simulation are $a = 0.5c/(f_{min}\sqrt{\epsilon_{r1}})$, $d = 1.07a$, $h = 0.5c/(f_{min}\sqrt{\epsilon_{r2}})$, and $Z_{TE_1} = 1/Y_1^{TE}$.
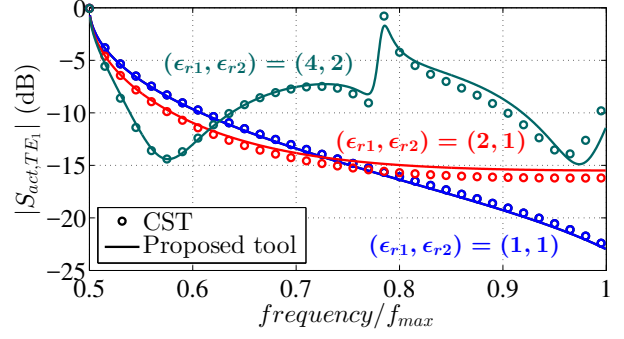

(a) Active S-parameters versus frequency for $\theta_0 = 30°$.

(b) Active S-parameters versus scan angles θ.

Fig. 6. Active S-parameters for TE_1-mode excitation versus frequency (a) and scan angles θ_0 (b) along the plane $\phi = 90°$ at $f_0 = (f_{min} + f_{max})/2$. The parameters used in the simulation are $a = 0.5c/(f_{min}\sqrt{\epsilon_{r1}})$, $d = 1.07a$, and $h = 0.5c/(f_{min}\sqrt{\epsilon_{r2}})$.

modes. The results shown in Fig. 6 illustrate that a very wideband performance is obtained for the TE_1 mode in both E- and H-plane. To give an example, for the case $\epsilon_{r1} = \epsilon_{r2} = 1$, the active S-parameter is less than -10 dB over a 48.8% band (refer to Fig. 6(a)) along the E-plane (i.e., at $\phi = 90°$), when the array is pointing at $\theta_0 = 30°$. On the other hand, Fig. 6(b) demonstrates a $\pm 51.9°$ scanning range.
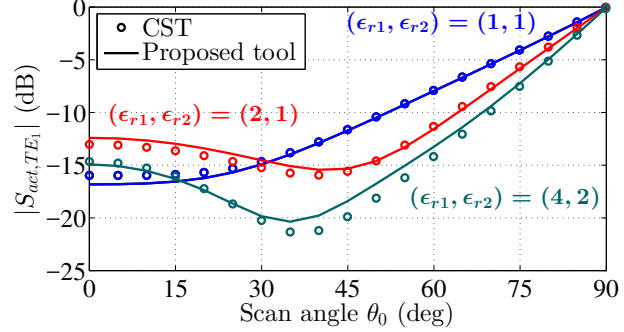
IV. RADIATION PATTERN

The computation of the radiation pattern in far-field zone has been carried out by considering the embedded element pattern of the array [16]. The goal of this section is to analyze advantages and limitations of the proposed CTS array for the generation of CP. It is worth mentioning that no pure CP can be achieved by employing the TEM and the TE_1 modes in the PPWs. In fact, as detailed in [15], the transverse E-field profile of the TE_1 mode presents a cosine-like distribution with respect to the x-component, whereas the E-field profile of the TEM mode is uniform all over the slot. This means that only at the center of each radiating slot the TEM and TE_1 modes can have equal amplitude. Conversely, the two modes are in quadrature by default [15].

A. Embedded element pattern

The far-field of the array is asymptotically evaluated [18]. A windowing approach is considered to truncate the current

along the $y-$axis direction [19]. Please note that this approach accounts for mutual coupling among array cells [16], [17].

Fig. 7 shows the embedded element pattern obtained by setting $f_{max} = 2f_{min}$, $a = 0.5c/(f_{min}\sqrt{\epsilon_1})$, $d_y = c/(30f_{min})$, $d = 1.07a$, and $\epsilon_{r1} = 1$ and considering no dielectric layer covering the slots. The array is steering the beam at broadside at the frequency $f_0 = (f_{min} + f_{max})/2$. The full-wave results were obtained computing the transverse field distribution of the two modes on the plane of the aperture and making them radiate in the upper half-space. The simulation setup adopted in the commercial software is shown in Fig. 2. Fig. 7 shows that there is an excellent agreement between full-wave results and our in-house tool.

B. Axial ratio

An important parameter to evaluate the purity of the CP generation is the axial ratio [18].

This preliminary study considers that the input power (i.e., $P_{tot} = 1W$) is equally splitted on each mode (i.e., TEM and TE_1). The scalar modal functions V_{inc}^{TEM} and $V_{inc}^{TE_1}$ in (7) and (10), respectively, are chosen accordingly, yielding:

$$V_{inc}^{TEm} = \sqrt{\frac{1}{Y_m^{TE}d_y}}, \quad m = \{0, 1\} \quad (15)$$

where $V_{inc}^{TE_0} = V_{inc}^{TEM}$. It is worth noting that the power ratio between the two modes can be optimized to improve the polarization purity of the antenna.
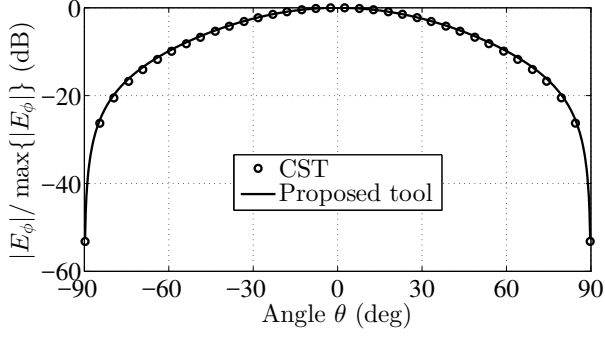
(a) E_ϕ-component in far-field region.
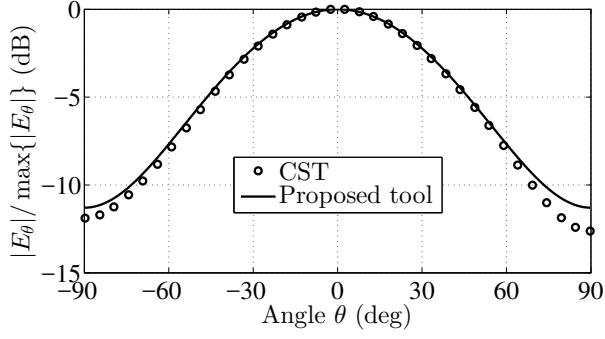
(b) E_θ-component in far-field region.

Fig. 7. Polar components of the embedded radiation pattern at the frequency $f_0 = (f_{min} + f_{max})/2$. The parameters used in the simulation are $a = 0.5c/\left(f_{min}\sqrt{\epsilon_{r1}}\right)$, and $d = 1.07a$.

(a) AR versus frequency along the main planes at $\theta_0 = 30°$.

(b) AR versus scan angles θ_0 at $f_0 = (f_{min} + f_{max})/2$.

Fig. 8. Axial ratio versus frequency (a) along the main planes at $\theta_0 = 30°$ and versus scan angles θ_0 (b) at $f_0 = (f_{min} + f_{max})/2$. The parameters used in the simulation are $a = 0.5c/\left(f_{min}\sqrt{\epsilon_{r1}}\right)$, and $d = 1.07a$.

The results have been validated by full-wave simulations and are shown in Fig. 8. The AR is lower than 1.5 dB over a 39.5% band (refer to Fig. 8(a)) and $\pm60°$ scanning range (refer to Fig. 8(b)) along the plane at $\phi = 90°$ at the central frequency. Table I presents a summary of the performance achieved by the design considered in this example. The parameters of the array are $\epsilon_{r1} = \epsilon_{r2} = 1$, $a = 0.5c/\left(f_{min}\sqrt{\epsilon_{r1}}\right)$, and $d = 1.07a$. The script BW_f stands for the frequency bandwidth of the infinite array under consideration and BW_θ for its scanning range at $f_0 = (f_{min} + f_{max})/2$. This summary relates to the beam-steering in the plane $\phi = 90°$. Such plane is the one generally used for scanning in CTS arrays [6] for parallel-fed architectures since it is devoid of grating lobes.
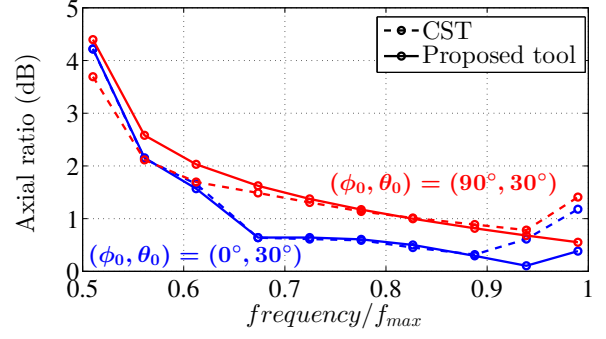
TABLE I
PERFORMANCE OF PROPOSED CTS SOLUTION

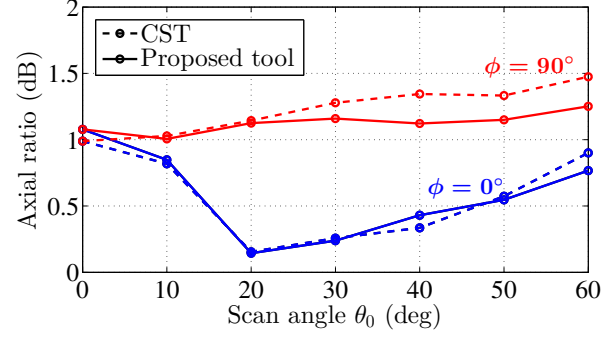|	$\mathbf{BW_f}$ (%)	$\mathbf{BW_\theta}$
$S_{act} < -10$ (dB)	48.8 *	$\pm51.9°$ **
$AR < 3$ (dB)	58.1 *	$\pm90°$ **
$AR < 1.5$ (dB)	39.5 *	$\pm60°$ **

* The array is steering the beam at $(\phi_0, \theta_0) = (90°, 30°)$;
** The reference frequency is $f_0 = (f_{min} + f_{max})/2$.

V. DESIGN GUIDELINES

This section discusses the choice of key design parameters and investigates the maximum achievable performance of the proposed array, in terms of bandwidth, impedance matching, scan range and axial ratio. This study relies on extensive parametric analyses performed using the fast in-house tool presented and validated. The obtained results confirm the broadband and wide-angle scanning capabilities of the proposed circularly-polarized CTS array.

A. Reflection coefficient

First, we study the impact of the geometry on the input matching. One can indeed determine the best d/a ratio between the array periodicity and the width of the slots by monitoring the active reflection coefficients for TEM and TE_1 modes, respectively. We take as a representative example a structure comprising air-filled PPWs that radiate in free space (i.e., $\epsilon_{r1} = \epsilon_{r2} = 1$) and we evaluate the performance for different scan angles in the planes $\phi = 0°$ and $\phi = 90°$. By using the tool presented in Section II, the active S-parameters when the array is fed by either a TEM or a TE_1 mode are plotted in Fig. 9. Let us remind that the width of the slots a of the proposed CTS array must be such that $\lambda/2 < a < \lambda$. This fact indicates that the active S-parameters may no longer be frequency-independent in the plane $\phi = 90°$, as for the case studied in [13]. In fact, the maps in Fig. 9 indicate that the best value of the ratio d/a is strongly dependent on the scanning range and the bandwidth one would like to achieve. The width of the slots a is taken as half the longest wavelength in the considered frequency range.
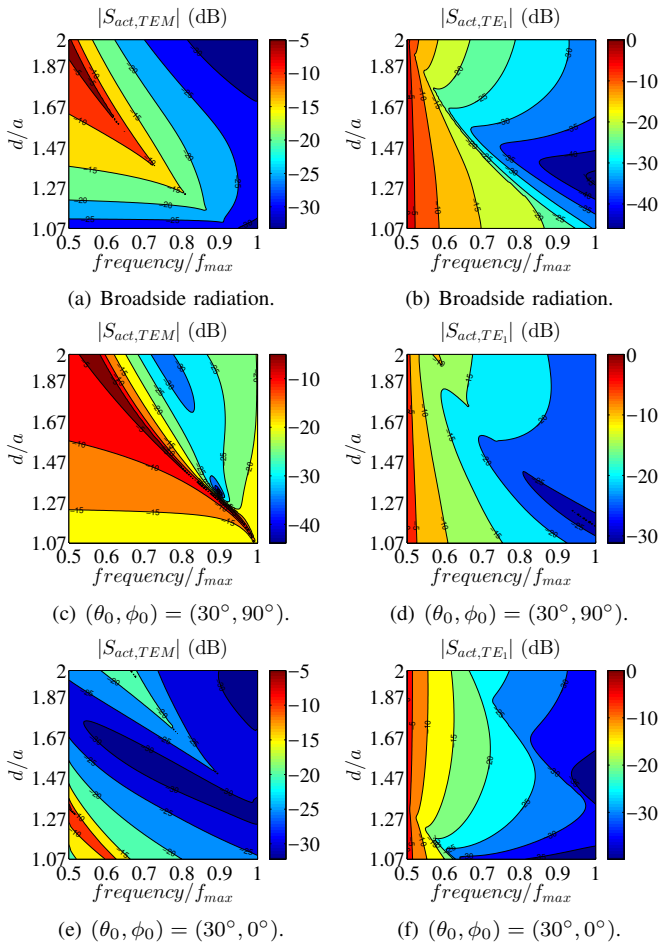
(a) Broadside radiation.

(b) Broadside radiation.

(c) $(\theta_0, \phi_0) = (30°, 90°)$.

(d) $(\theta_0, \phi_0) = (30°, 90°)$.

(e) $(\theta_0, \phi_0) = (30°, 0°)$.

(f) $(\theta_0, \phi_0) = (30°, 0°)$.

Fig. 9. Maps of the active S-parameter as a function of frequency and the ratio d/a for both TEM ((a), (c), and (e)) and TE_1 ((b), (d), and (f)) modes. The air-filled PPWs radiate in free space. Several scan angles in the planes $\phi_0 = 0°$ and $\phi_0 = 90°$ are considered.

(a) Broadside radiation.

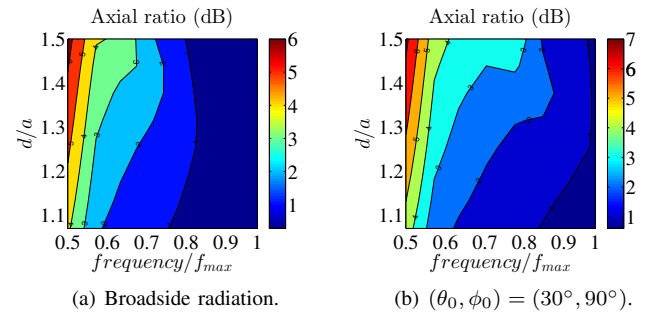(b) $(\theta_0, \phi_0) = (30°, 90°)$.

Fig. 10. Maps of the AR as a function of frequency and the ratio d/a. The air-filled PPWs radiate in free space. (a) Broadside array. (b) Array steering the beam at $\theta_0 = 30°$ along the plane $\phi_0 = 90°$.

B. Circular polarization

Finally, the behavior of the axial ratio as a function of frequency and d/a ratio is studied to draw design guidelines for high-purity circularly polarized radiation. The slots are still considered as being air-filled and radiate in free space (i.e., $\epsilon_{r1} = \epsilon_{r2} = 1$). Fig. 10(a) reports the parametric study when the array is steering the beam at broadside, whereas Fig.10(b) shows the results for pointing at $(\phi_0, \theta_0) = (90^o, 30^o)$. We can first notice that the AR gets worse as the scan angle θ_0 is different from zero. Moreover, AR decreases when $f/f_{max} \to 1$, as the cut-off frequency of the TE_1 mode is fixed at the lowest frequency. It is also worth noting that this condition mitigates issues due to the dispersion between the TEM and TE_1 modes within the PPWs.

The results above imply that the AR performance improves as the ratio d/a is such that $d/a \to 1$. This trend is intuitive because a smaller array periodicity implies lower side lobe levels in far-field zone. However, as discussed in Section V-A, low values of d/a penalize the input matching when the array is excited by a TE mode, especially at low frequencies. Thus, the optimal sizing relies on specific design goals. A practical case study is discussed in Section VI.

VI. FINITE-SIZE ARRAY DESIGN

The goal of this section is to show a representative example of a possible design by using the guidelines provided in Section V. The antenna performance is monitored within the frequency range 20-40 GHz. The dual-mode CTS array consists of four air-filled radiating slots that radiate in free space. The length of the slots along $y-$axis is $d_y = 5\lambda_{max} \sim 74.9$ mm, whereas their width is $a = 0.5c/(f_{min}) \sim 7.49$ mm. About the choice of the array periodicity d, a trade-off occurs between the input matching and axial ratio performance, as detailed in Section V-B. Recalling the arguments in Section V-A, the best sizing for the input matching is given by $1.1 < d/a < 1.4$ while scanning along $\phi = 90°$. On the contrary, the largest axial ratio bandwidth operation is for $d/a \to 1$. Thus, the best choice for the array periodicity is $d = 1.1a \sim 8.20$ mm.

The input reflection coefficient of the slots is displayed in Fig. 11 as function of both frequency and scan angles under TEM and TE_1 mode operation, respectively. It is worth noting that the input reflection coefficient is computed in an infinite

To give an idea, when the array is steering the beam at broadside, the trend is that the best matching for the TEM mode is obtained by choosing $d/a \to 1$, as shown in Fig. 9(a), whereas for TE_1 mode by value of d/a as large as possible (see Fig. 9(b)). In particular, the active reflection coefficient is smaller than -10 dB by choosing d/a such that $1 < d/a \leq 1.4$, in case of TEM mode excitation. On the contrary, the best input matching when the array is fed by TE_1 modes is reached for $d/a \approx 1.92$. Thus, the stricter constraint is imposed by TEM mode configuration and a good trade-off sizing is found choosing $d/a \approx 1.4$.

To conclude, let us focus on the $\phi = 90°$ plane, where no grating lobes occur. As shown in Fig. 9(c) and Fig. 9(d), the trend is the same as for broadside radiation. In this case, $|S_{act}| < -10$ dB is given by choosing $d/a \approx 1.1$ for TEM mode and $d/a \approx 1.96$ for TE_1 mode. This means that the ratio between array period and width of the slots achieving the largest bandwidth operation is, in this case, $d/a \approx 1.1$. For sake of completeness, we report also the maps along the plane $\phi = 0°$ in Fig. 9(e) and Fig. 9(f).
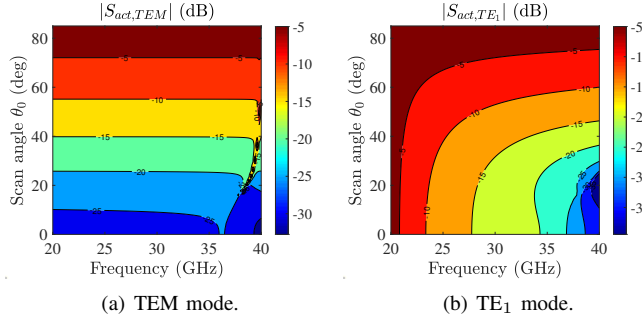
(a) TEM mode.

(b) TE$_1$ mode.

Fig. 11. Maps of the input reflection coefficient as a function of frequency and the scan angles θ_0. The air-filled PPWs radiate in free space. (a) TEM and (b) TE$_1$ mode operation. The array is steering the beam along the plane $\phi_0 = 90°$.

periodic environment. Fig. 11(a) confirms the flat behaviour of the active input impedance for TEM mode operation. This result is also valid in a monomodal enviroment, as detailed in [13]. As shown in Fig. 11(b), the TE$_1$ mode operation limits the antenna performance since its frequency response worsens at low frequencies due to the location of the cut-off frequency of the TE$_1$ mode at $f_{min} = 20$ GHz. Furthermore, the input reflection coefficient worsens in scanning for both modes. Thus, it follows that the largest bandwidth operation shows up at broadside where the relative bandwidth is about 52.9%. Besides, a wide scanning range is observed as well. Indeed, the active reflection coefficient $|S_{act}|$ is lower than -10 dB in a 40.8% relative bandwidth when the array steers its main beam at $\theta_0 = 45°$ in the plane $\phi = 90°$ (see Fig. 11).

The E-field polar components are calculated using a windowind approach as in Section IV and are plotted at the central frequency $f_0 = 30$ GHz for different scan angles in Fig. 12(a)-(b). The axial ratio is also plotted as function of the scan angle θ_0 in Fig. 12(c). From Fig. 12(a)-(b), a $\sim$ 3 dB scan loss is observed while scanning at 45°. Such dual-mode CTS array is then classifiable as wide-scanning antenna [20]. Furthermore, it is also clear from Fig. 12(a)-(b) that the two modes radiate two far-field orthogonal components. This is evident by looking at the end-fire radiation: E_ϕ presents a null radiation at the end-fire direction since the TE$_1$ mode has a cosine-like profile over the $x-$axis direction of the slots (i.e., null at the edges); on the contrary, E_θ is non-null at the end-fire direction since the TEM mode has an uniform distribution along the radiating slots. Moreover, it can be noticed from Fig. 12(c) that the scanning range for which $AR < 3$ dB is up to $\pm 76°$ at 30 GHz in the plane $\phi = 90°$.

Besides, the axial ratio is plotted as function of frequency and scan angle θ_0 in Fig. 13. By varying the scan angle along the plane $\phi = 90°$, the axial ratio is computed in the pointing direction of the array. The results show that the AR frequency bandwidth is stable almost all over the entire scanning range of investigation. In other words, the AR does not significantly deteriorate with scan losses. This is clearly visible from Fig. 12(a) and (b): the maximum amplitude of the two far-field orthogonal components are reduced simultaneusly in scanning. Thus, as shown in Fig. 12(c), the AR is lower than 3 dB around the pointing angle of the array. This means that the

(a) $\phi-$component.

(b) $\theta-$component.
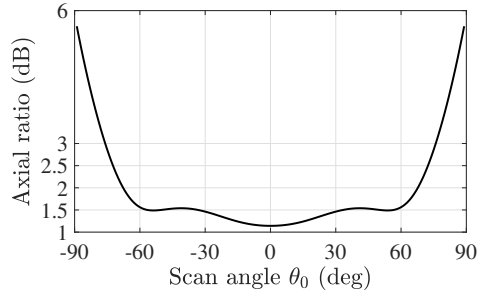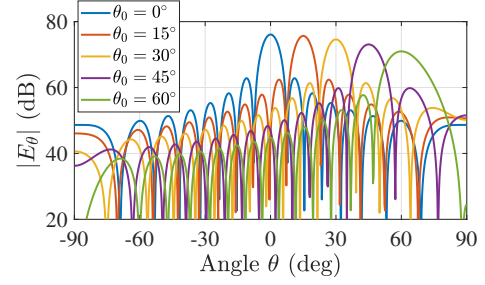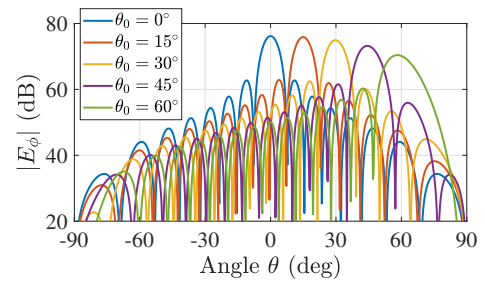
(c) Axial ratio.

Fig. 12. (a), (b) Polar components of the radiation pattern at the frequency $f_0 = 30$ GHz for different scan angles. (c) Axial ratio versus scan angle θ_0 at the frequency $f_0 = 30$ GHz. The array is steering the beam along the plane $\phi_0 = 90°$.

antenna performance is mainly curtailed by the input matching behaviour under TE$_1$ mode operation.

Fig. 13. Axial ratio as a function of frequency and scan angle θ_0. The air-filled PPWs radiate in free space. The array is steering the beam along the plane $\phi_0 = 90°$.

Fig. 14. Maps of the AR as function of the power ratio P_{TEM}/P_{TE_1} and (a) frequency for broadside radiation or (b) scan angle θ_0 at the central frequency $f_0 = 30$ GHz. The air-filled PPWs radiate in free space. The array is steering the beam along the plane $\phi_0 = 90°$.

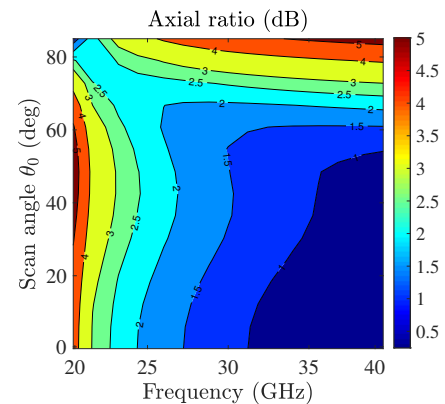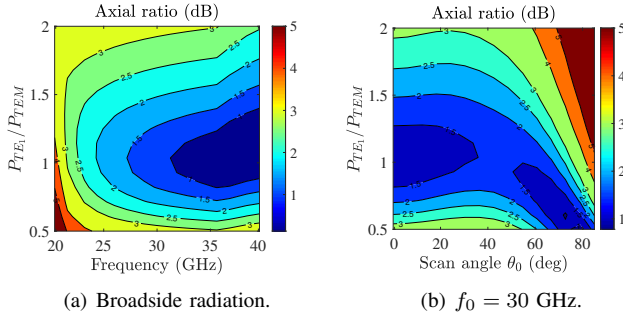To conclude, it is worth noting that the input matching of the antenna might be improved by placing dielectric layers on the top of the slots [26]. As an example, Fig. 6(a) shows that placing a dielectric layer of relative permittivity $\epsilon_{r2} = 2$ slightly improves the antenna matching when the slots are fed by the TE$_1$ mode.

A. Input power optimization

Section IV-B analyzes the radiation properties of the antenna by considering half of the input power for TEM and TE$_1$ mode excitation, respectively. In this case, a voltage excitation given by (15), corresponding to a unitary overall input power, was considered for each mode. Nevertheless, this may not be the optimum power split between the two feeding modes. Indeed, the amplitudes of the impinging modes can be optimized in order to further improve the AR performance of the antenna. The amplitudes of the voltage waves of the input modes are related to their power ratio as follows

$$V_{inc}^{TE_1} = V_{inc}^{TEM} \sqrt{\frac{Z_1^{TE}}{\eta_0}} \sqrt{\frac{P_{TE_1}}{P_{TEM}}} \qquad (16)$$

where η_0 and Z_1^{TE} are the free space and TE$_1$ mode characteristic impedances, respectively, whereas P_{TEM} and P_{TE_1} are the input power of TEM and TE$_1$ modes, respectively. By enforcing the amplitude of TEM mode V_{inc}^{TEM} such that the maximum input power is $P_{tot} = P_{TEM} + P_{TE_1} = 1$ W, the ratio P_{TE_1}/P_{TEM} may be varied to analyze the AR performance of the array. This analysis is reported in Fig. 14. In particular, in Fig. 14(a) the frequency behaviour of the dual-mode CTS array is studied when the beam is steered at broadside. In Fig. 14(b) the AR is plotted versus the scan angle θ_0 at the central frequency $f_0 = 30$ GHz. From Fig. 14(a), it turns out that the best power split is achieved for $P_{TE_1}/P_{TEM} \sim 1.1$ which is rather close to the case previously analyzed (i.e., total power equally splitted for the two feeding modes). On the other hand, for scanning at a defined frequency of operation, from Fig. 14(b) it emerges that the optimum power split for maximizing the scan range at 30 GHz is given by $P_{TE_1}/P_{TEM} \sim 0.82$. However, as explained in the first part of this section, the input matching of the antenna is satisfactory up to $\pm 45°$ in the plane $\phi = 90°$.

Such a scanning range is easily achieved for equal power division between the two feeding modes. Specifically, when $P_{TE_1}/P_{TEM} = 1$ the proposed dual-mode CTS array exhibits an AR lower than 3 dB up to $\pm 75.8°$ at the central frequency $f_0 = 30$ GHz.

B. Feeding system

In this sub-section, we briefly discuss a possible feeding system of the circularly-polarized CTS array. A dual-mode pillbox coupler, inspired by the architectures presented in [30], [31], can be designed to excite a corporate feed-network made of bimodal longitudinally-corrugated PPWs (LCPPWs). The unit-cell of a LCPPW line is depicted in Fig. 15. We restrict our analysis to PPWs with height between half a wavelength and a wavelength. The use of LCPPWs is needed in order to decouple the TEM and TM$_1$ modes since this latter is degenerate with the TE$_1$ mode [21]–[25]. In particular, the TE$_1$ and TM$_1$ modes are orthogonally-polarized and then they do not couple. On the other hand, TEM and TM$_1$ modes have the same field orientation and can easily couple each other. This is clear by comparing the dispersion diagrams of conventional and longitudinally-corrugated PPW lines as shown in Fig. 16(a) and (b), respectively. Both PPW and LCPPW lines are filled with air. The geometrical parameters of the LCPPW unit-cell are $h_{TE_1} = 0.5\lambda_{max} \sim 7.49$ mm, $h_{TEM} = 0.5\lambda_{min} \sim 2.99$ mm, $w_{corr} = \lambda_{max}/20 \sim 0.74$ mm, and $p_{corr} = \lambda_{max}/10 \sim 1.49$ mm. In Fig. 16, it can be noticed that the fundamental TEM mode is non-dispersive in both PPW and LCPPW lines. Moreover, using LCPPWs the TE$_1$ and TM$_1$ modes are no longer degenerate. The structure operates in a bi-modal regime within the bandwidth 23.5-38.3 GHz. The corrugations slightly shift the cut-off frequencies of LCPPW modes with respect to those of standard PPWs.
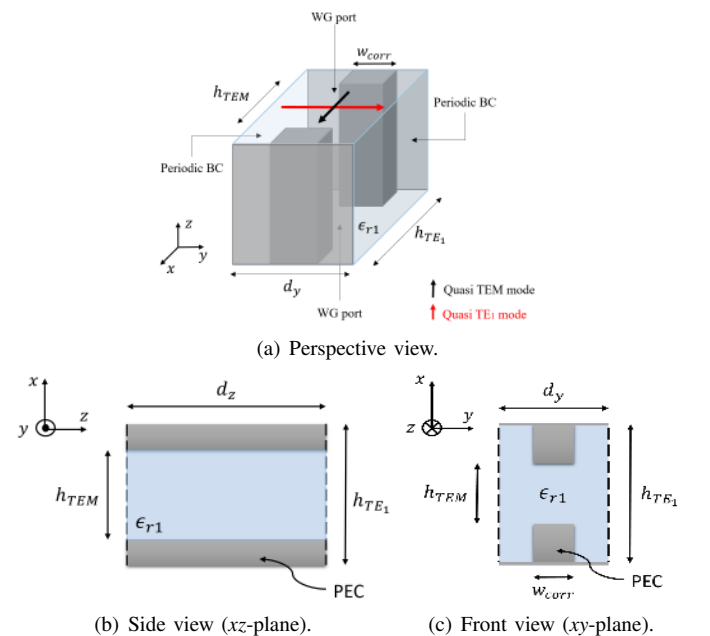

(a) Perspective view.

(b) Side view (xz-plane).　　(c) Front view (xy-plane).

Fig. 15. Unit-cell of the dual-mode LCPPW. The structure is periodic along y-axis direction. (a) Perspective view. (b) xz-plane view. (c) xy-plane view.
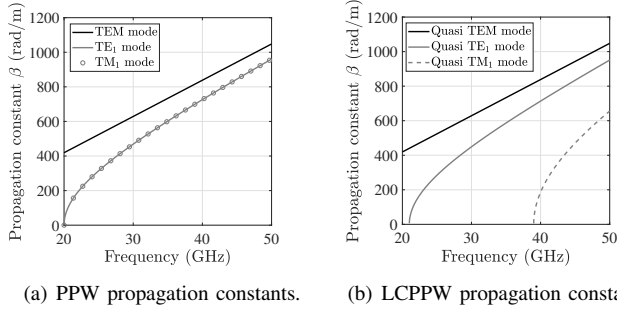
(a) PPW propagation constants.

(b) LCPPW propagation constants.

Fig. 16. Dispersion diagram of TEM, TE_1, amd TM_1 modes. (a) PPW and (b) LCPPW.

As result, the effective operative bandwidth is reduced from 66.6% to 50.1%. A summary of the cut-off frequencies of different modes is presented for both conventional PPW and LCPPW in Table II.

Additionally, the slots can be fed using coaxial probes or crossed dipoles placed in the very proximity of the aperture [27]–[29]. The latter solution helps in mitigating the different dispersive behaviour of TEM and TE_1 modes. Indeed, the inter-modal dispersion occuring between TEM and TE_1 modes is alleviated either feeding the slots as close as possible to the radiating aperture or at higher frequencies (see Fig. 16). The latter observation also emerged from the study carried out in this paper. Thus, the results presented in Section VI will be not be strongly affected by considering the dispersion and the feeding system of the antenna. Therefore, the authors believe that this contribution gives a valid starting point to address the design of such proposed dual-mode CTS array. In other words, in this section we proposed some ideas to engineer the dispersion and the feeding system of the antenna. Note that there might be several other ways in addition to the ones proposed here.

TABLE II
CUT-OFF FREQUENCIES COMPARISON BETWEEN PPW AND LCPPW

	PPW	LCPPW
TEM mode	$f_{co,TEM}^{PPW} = 0$ Hz	$f_{co,TEM}^{LCPPW} = 0$ Hz
TE_1 mode	$f_{co,TE_1}^{PPW} = 0.5 f_{max}$	$f_{co,TE_1}^{LCPPW} = 0.59 f_{max}$
TM_1 mode	$f_{co,TM_1}^{PPW} = 0.5 f_{max}$	$f_{co,TM_1}^{LCPPW} = 0.96 f_{max}$

* The symbols $f_{co,m}^{PPW}$ and $f_{co,m}^{LCPPW}$ represent the cut-off frequencies of the m-th mode in conventional and longitudinally corrugated PPW, respectively.

VII. CONCLUSION

An in-depth study of a novel circularly-polarized CTS array has been presented. The array is based on long radiating slots fed by over-moded PPW lines. Two orthogonally-polarized modes (i.e., TEM and TE_1) are employed to feed a shared radiating aperture and, thus, generate circularly-polarized fields in the far-field zone. A fast in-house numerical tool has been developed to address an efficient analysis of this class of CTS arrays. In particular, the tool is able to provide the active reflection coefficient and radiation properties of open-ended over-moded stubs, when both TEM and TE_1 mode excitations are considered. The proposed analysis method is then used to highlight advantages and limitations of this new antenna concept focusing on the array performance, and to provide design guidelines. The AR of the radiated field is evaluated for broadside radiation and scanning along the principal planes of the array. All the results have been validated by full-wave simulations, showing a very good agreement. It has been demonstrated that the presented circularly-polarized CTS array architecture is suitable for wideband, wide-angle scanning applications. More precisely, the AR is lower than 3 dB over a 52.9% relative bandwidth for broadside radiation. Furthermore, the active input reflection coefficient $|S_{act}|$ is lower than -10 dB over a 40.8% relative bandwidth when the array steers its main beam at $\theta_0 = 45°$ along the plane parallel to the slots. Furthermore, practical designs of finite arrays have been discussed and several solutions to excite the array minimizing the intermodal dispersion have been presented. The small form factor and low profile of the antenna make such architecture an interesting candidate for the next generation of satellite communication systems, in particular, for Ka-band terminals in Satcom applications.

APPENDIX A
ACTIVE ADMITTANCE FOR TE_1 MODE

The mathematical expression of the normalized active admittance for TE_1 mode is given by

$$\bar{Y}_{act}^{TE_1} = -\frac{1}{\left|V_1^{TE}\sqrt{a}\right|^2}\left[\Psi_{1x}^{TE_1} + \Psi_{2x}^{TE_1} + \Psi_{1y}^{TE_1} + \Psi_{2y}^{TE_1}\right] \tag{IA.1}$$

where

$$\Psi_{1x}^{TE_1} = -\frac{\sqrt{\frac{2}{a}}\frac{\pi}{a}\left(V_1^{TE}\right)^*}{d\sqrt{k_{y0}^2 + (\pi/a)^2}}\sum_{m=1}^{M-1}\left(\frac{c_m^{TM}}{Y_m^{TM}}V_m^{TM} - \frac{c_m^{TE}}{Y_m^{TE}}V_m^{TE}\right)$$
$$\times \sum_{n=-N_f}^{N_f}\Gamma_m(k_{xn})\tilde{G}_{xx}^{HM}\Gamma_1(-k_{xn}) \tag{IA.2}$$

$$\Psi_{2x}^{TE_1} = -\frac{\sqrt{\frac{2}{a}}\frac{\pi}{a}\left(V_1^{TE}\right)^*}{d\sqrt{k_{y0}^2 + (\pi/a)^2}}\sum_{m=0}^{M-1}\left(\frac{b_m^{TM}}{Y_m^{TM}}V_m^{TM} - \frac{b_m^{TE}}{Y_m^{TE}}V_m^{TE}\right)$$
$$\times \sum_{n=-N_f}^{N_f}\Lambda_m(k_{xn})\tilde{G}_{xy}^{HM}\Gamma_1(-k_{xn}) \tag{IA.3}$$

$$\Psi_{1y}^{TE_1} = \frac{\sqrt{\frac{2}{a}}ik_{y0}\left(V_1^{TE}\right)^*}{d\sqrt{k_{y0}^2 + (\pi/a)^2}}\sum_{m=1}^{M-1}\left(\frac{c_m^{TM}}{Y_m^{TM}}V_m^{TM} - \frac{c_m^{TE}}{Y_m^{TE}}V_m^{TE}\right)$$
$$\times \sum_{n=-N_f}^{N_f}\Gamma_m(k_{xn})\tilde{G}_{yx}^{HM}\Lambda_1(-k_{xn}) \tag{IA.4}$$

$$\Psi_{2y}^{TE_1} = \frac{\sqrt{\frac{2}{a}}ik_{y0}\left(V_1^{TE}\right)^*}{d\sqrt{k_{y0}^2 + (\pi/a)^2}} \sum_{m=0}^{M-1} \left(\frac{b_m^{TM}}{Y_m^{TM}} V_m^{TM} - \frac{b_m^{TE}}{Y_m^{TE}} V_m^{TE} \right)$$

$$\times \sum_{n=-N_f}^{N_f} \Lambda_m(k_{xn}) \tilde{G}_{yy}^{HM} \Lambda_1(-k_{xn})$$

(IA.5)

where Y_m^{TE} and Y_m^{TM} are the wave admittance of TE and TM modes, respectively, in PPW and the expressions of $\Gamma(k_x)$, $\Lambda(k_x)$, c_m^{TE}, c_m^{TM}, b_m^{TE}, and b_m^{TM} can be found in [13]. Moreover, $k_{xn} = k_{x0} + 2\pi n/d$ and G_{ij}^{HM} is the Fourier transform of the (i,j)-th entry of the Green's dyad $\underline{\underline{G}}^{HM}$.

REFERENCES

[1] R. A. Pearson, J. Vazquez, M. W. Shelley, A. Payne, V. Stoiljkovic, and M. Steel, "Next generation mobile SATCOM terminal antennas for a transformed world," *Proc. 5th Eur. Conf. Antennas Propag. (EUCAP)*, Rome, 2011, pp. 2341-2345.

[2] W. W. Milroy, "The continuous transverse stub (CTS) array: Basic theory, experiment, and application," in *Proc. Antenna Appl. Symp.*, 2527, 1991, vol. 2, pp. 253283.

[3] W. W. Milroy, "Continuous transverse stub element devices for flat plate antenna arrays," U.S. Patent 5 483 248, Jan. 9, 1996.

[4] W. W. Milroy, "Antenna array configurations employing continuous transverse stub elements," U.S. Patent 5 412 394, May 2, 1995.

[5] H. Choe, and S. Lim, "Millimeter-wave continuous transverse stub (CTS) antenna array using substrate integrated waveguide (SIW) technology," *IEEE Trans. Antennas Propag.*, vol. 62, no. 11, pp. 5497-5503, Nov. 2014.

[6] M. Ettorre, F. Foglia Manzillo, M. Casaletti, R. Sauleau, L. Le Coq, and N. Capet, "Continuous transverse stub array for Ka-band applications," *IEEE Trans. Antennas Propag.*, vol. 63, no. 11, pp. 4792-4800, Nov. 2015.

[7] F. Foglia Manzillo, M. Ettorre, M. S. Lahti, K. T. Kautio, D. Lelaidier, E. Seguenot, and R. Sauleau, "A multilayer LTCC solution for integrating 5G access point antenna modules," *IEEE Trans. Microw. Theory Tech.*, vol. 64, no. 7, pp. 2272-2283, Jul. 2016.

[8] A. Neto, and J. J. Lee, "Ultrawide-band properties of long slot arrays," *IEEE Trans. Antennas Propag.*, vol. 54, no. 2, pp. 534-543, Feb. 2006.

[9] R. Dybdal, *Communication satellite antennas: system architecture, technology, and evaluation.* McGraw-Hill, 2009.

[10] M.-A. Joyal, and J.-J. Laurin, "Analysis and design of thin circular polarizers based on meander lines," *IEEE Trans. Antennas Propag.*, vol. 60, no. 6, pp. 3007-3011, Jun. 2012.

[11] S. M. A. Momeni Hasan Abadi, and N. Behdad, "Wideband linear-to-circular polarization converters based on miniaturized-element frequency selective surfaces," *IEEE Trans. Antennas Propag.*, vol. 64, no. 2, pp. 525-534, Feb. 2016.

[12] Y. J. Cheng, J. Wang, and X. L. Liu, "94 GHz substrate integrated waveguide dual-circular-polarization shared-aperture parallel-plate long-slot array antenna with low sidelobe level," *IEEE Trans. Antennas Propag.*, vol. 65, no. 11, pp. 5855-5861, Nov. 2017.

[13] F. Foglia Manzillo, M. Ettorre, M. Casaletti, N. Capet, and R. Sauleau, "Active impedance of infinite parallel-fed continuous transverse stub arrays," *IEEE Trans. Antennas Propag.*, vol. 63, no. 7, pp. 3291-3297, Jul. 2015.

[14] L. B. Felsen, and N. Marcuwitz, *Radiation and scattering of waves.* Hoboken, NJ, USA: Wiley/IEEE Press, 1994.

[15] D. M. Pozar, *Microwave engineering - 3th ed..* John Wiley & Sons, 2005, ch. 3.2.

[16] D. M. Pozar, "The active element pattern," *IEEE Trans. Antennas Propag.*, vol. 42, no. 8, pp. 1176-1178, Aug 1994.

[17] W. P. M. N. Keizer, "Planar phased-array antennas: mutual coupling and ultralow peak sidelobes," *IEEE Antennas Propag. Magazine*, vol. 61, no. 1, pp. 14-28, Feb. 2019.

[18] C. A. Balanis, *Antenna theory: analysis and design.* Wiley-Interscience, 2005.

[19] A. Ishimaru, R. Coe, G. Miller, and W. Geren, "Finite periodic structure approach to large scanning array problems," *IEEE Trans. Antennas Propag.*, vol. 33, no. 11, pp. 1213-1220, Nov. 1985.

[20] J. A. Kasemodel, C. Chen and J. L. Volakis, "Wideband planar array with integrated feed and matching network for wide-angle scanning," *IEEE Trans. Antennas Propag.*, vol. 61, no. 9, pp. 4528-4537, Sep. 2013.

[21] P. S. Kildal, "Artificially soft and hard surfaces in electromagnetics," *IEEE Trans. Antennas Propag.*, vol. 38, no. 10, pp. 1537-1544, Oct. 1990.

[22] A. E. Karbowiak, "Theory of imperfect waveguides: the effect of wall impedance," *Proc. of the IEE - Part B: Radio and Electronic Engineering*, vol. 102, no. 5, pp. 698-708, Sep. 1955.

[23] R. B. Dybdal, L. Peters, and W. H. Peake, "Rectangular waveguides with impedance walls," *IEEE Trans. Microw. Theory Tech.*, vol. 19, no. 1, pp. 2-8, Jan. 1971.

[24] M. Ng Mou Kehn, "Modal analysis of all-walls longitudinally corrugated rectangular waveguides using asymptotic corrugations boundary conditions," *IEEE Trans. Microw. Theory Tech.*, vol. 61, no. 11, pp. 3821-3837, Nov. 2013.

[25] L. W. Epp, D. J. Hoppe, and D. T. Kelley, "A TE/TM modal solution for rectangular hard waveguides," *IEEE Trans. Microw. Theory Tech.*, vol. 54, no. 3, pp. 1048-1054, Mar. 2006.

[26] E. Magill, and H. Wheeler, "Wide-angle impedance matching of a planar array antenna by a dielectric sheet," *IEEE Trans. Antennas Propag.*, vol. 14, no. 1, pp. 49-53, Jan. 1966.

[27] M. Ettorre, W. A. Alomar, and A. Grbic, "2-D Van Atta array of wideband, wideangle slots for radiative wireless power transfer systems," *IEEE Trans. Antennas Propag.*, vol. 66, no. 9, pp. 4577-4585, Sep. 2018.

[28] S. Zhou, M. Ettorre, and A. Grbic, "An 8×4 continuous transverse stub array fed by coaxial ports," *IEEE Antennas Wireless Propag. Lett.*, vol. 18, no. 6, pp. 1303-1307, June 2019.

[29] R. J. Bolt, D. Cavallo, G. Gerini, D. Deurloo, R. Grooters, A. Neto, and G. Toso, "Characterization of a dual-polarized connected-dipole array for Ku-band mobile terminals," *IEEE Trans. Antennas Propag.*, vol. 64, no. 2, pp. 591-598, Feb. 2016.

[30] R. Sauleau and M. Ettorre "Multilayer pillbox type parallel-plate waveguide antenna and corresponding antenna system", U.S. Patent 9 246 232, Jan. 26, 2016.

[31] M. Ettorre, R. Sauleau, and L. Le Coq, "Multi-beam multi-layer leaky-wave SIW pillbox antenna for millimeter-wave applications," *IEEE Trans. Antennas Propag.*, vol. 59, no. 4, pp. 1093-1100, Apr. 2011.

[32] CST STUDIO SUITE®, CST Computer Simulation Technology, 2017.